Gating mechanism of human N-type voltage-gated calcium channel

Yanli Dong[1,3]*, Yiwei Gao[1,3]*, Shuai Xu[4]*, Yuhang Wang[1,3], Zhuoya Yu[1,3], Yue Li[1,3], Bin Li[1,3], Bei Yang[1,3], Xuejun Cai Zhang[1,3], Daohua Jiang[5]**, Zhuo Huang[4,6]**, Yan Zhao[1,2,3]**

[1] National Laboratory of Biomacromolecules, CAS Center for Excellence in Biomacromolecules, Institute of Biophysics, Chinese Academy of Sciences, Beijing 100101, China

[2] State Key Laboratory of Brain and Cognitive Science, Institute of Biophysics, Chinese Academy of Sciences, 15 Datun Road, Beijing, 100101, China

[3] College of Life Sciences, University of Chinese Academy of Sciences, Beijing 100049, China

[4] State Key Laboratory of Natural and Biomimetic Drugs, Department of Molecular and Cellular Pharmacology, School of Pharmaceutical Sciences, Peking University Health Science Center, Beijing, 100191, China

[5] Laboratory of Soft Matter Physics, Institute of Physics, Chinese Academy of Sciences, Beijing 100190, China

[6] IDG/McGovern Institute for Brain Research, Peking University, Beijing, 100871, China

* These authors contribute equally to this project.

** Correspondence emails: zhaoy@ibp.ac.cn (Y.Z.), huangz@hsc.pku.edu.cn (Z.H.), jiangdh@iphy.ac.cn (D.J.)

Abstract

N-type voltage-gated calcium (Ca_V) channels mediate Ca^{2+} influx at the presynaptic terminals in response to action potential and play vital roles in synaptogenesis, neurotransmitter releasing, and nociceptive transmission. Here we elucidate a cryo-electron microscopy (cryo-EM) structure of the human $Ca_V2.2$ complex at resolution of 2.8 Å. This complex structure reveals how the $Ca_V2.2$, $\beta1$, and $\alpha2\delta1$ subunits are assembled. In our structure, the second voltage-sensing domain (VSD) is stabilized at a resting-state conformation, which is distinct from the other three VSDs of $Ca_V2.2$ as well as activated VSDs observed in previous structures of Ca_V channels. The structure also shows that the intracellular gate formed by S6 helices is closed, and a W-helix from the DII-III linker is determined to act as a blocking-ball that causes closed-state inactivation in $Ca_V2.2$. Collectively, our structure provides previously unseen structural insights into fundamental gating mechanisms of Ca_V channels.

Introduction

Voltage-gated calcium channels (Ca_V channels) are a type of essential mediators to convert action potential into influx of Ca^{2+} ions, a crucial secondary messenger to regulate a variety types of cellular events, such as muscle contraction, secretion of the neurotransmitters, cell division, differentiation, and apoptosis [1-4]. Ca_V channels are generally categorized into two groups according to their activation threshold, i.e., high-voltage activated (HVA) and low-voltage activated (LVA) Ca_V channels. Based on their sequence homology, Ca_V channels in mammals contain ten members, which are further classified into three subfamilies (Ca_V1, Ca_V2, and Ca_V3) and six types (L-, P/Q-, N-, R-, T-types) [5-7]. The N-type Ca_V channel, also called $Ca_V2.2$, is a HVA channel, belongs to the Ca_V2 subfamily (containing P/Q-, N-, and R-type), and is exclusively expressed in the central and peripheral neurons [8]. The $Ca_V2.2$ is predominantly located in the pre-synaptic terminals and mediates the Ca^{2+} influx that triggers neurotransmitter release at the fast synapses [9,10]. Dysfunctions of $Ca_V2.2$ channels alter neuronal functions and lead to diseases, such as myoclonus-dystonia-like syndrome [11]. Moreover, the $Ca_V2.2$ channel plays a critical role in spinal nociceptive signaling, and thus it has become an important drug target for chronic pain treatment.

Molecular mechanisms of the Ca_V channels have been studied extensively for decades, including recent structural studies of L-type $Ca_V1.1$ isolated from rabbit skeletal muscle [12-15] and human T-type $Ca_V3.1$ [16]. These studies revealed structural features of the Ca_V channels at their inactivated state with all the voltage sensing domains (VSD_I–VSD_{IV}) adopting an activated 'up' conformation. The structures of the $Ca_V1.1$ complex also elucidate the assembly of Ca_V channel with auxiliary β and $\alpha2\delta$ subunits. A range of ligands were determined in complexes with $Ca_V1.1$ or $Ca_V3.1$, and these structural studies provide molecular bases for ligand recognition and facilitate further rational drug development targeting Ca_V channels. Despite these advances in structural studies on the Ca_V channels, more structural insight is desirable to fully understand the molecular mechanism of the $Ca_V2.2$ channel from structural untouched Ca_V2 subfamily, because not only it shares low sequence identity with the available structures from the other two subfamilies, but also

some fundamental mechanistic questions remain to be addressed. For example, whereas the available structures of Ca_V channels are featured with activated VSDs [12-14,16], these VSDs at their resting state appear to be required to fully understand the channel gating mechanism. Moreover, the $Ca_V2.2$ harbors a distinct closed-state inactivation during repolarization [17-19] and is modulated by phosphatidylinositol 4,5-bisphosphate (PIP_2) molecules [20-25]. These underlying molecular mechanisms need further investigation to elucidate.

Here, we purified the recombinant human $Ca_V2.2$ (also called α-subunit) in complex with the $\beta1$ and $\alpha2\delta1$ subunits, and determined their complex structure using single particle cryo-EM method. This structure reveals the first view of asymmetric activation of the four VSDs with the VSD_{II} at its resting state, presumably locked by a PIP_2-like lipid molecule. Furthermore, we identify a unique α-helix that blocks the intracellular gate of $Ca_V2.2$, contributing to the close-state inactivation of the $Ca_V2.2$. These results enable us to gain significant novel insights into the activation and inactivation mechanisms of human Ca_V channels.

Results and discussion

Structure determination and architecture of the $Ca_V2.2$ complex

To investigate the architecture of the N-type $Ca_V2.2$ complex, we co-expressed human N-terminal truncated $Ca_V2.2$, full-length wild type (WT) $\alpha2\delta1$, and full-length WT $\beta1$ in HEK 293 cells. To monitor the expression of the complex during purification, the $Ca_V2.2$ was fused with a C-terminal GFP-Twinstrep tag. In order to enhance the expression level, the intrinsically disordered N-terminal region (residues 1–64) was truncated, and we denote this construct as $Ca_V2.2^{EM}$. We carried out whole-cell patch clamp experiments in HEK 293T cells to characterize the channel properties of both human WT full-length $Ca_V2.2$ and $Ca_V2.2^{EM}$ constructs, in the presence of auxiliary $\beta1$ and $\alpha2\delta1$ subunits. The $Ca_V2.2^{EM}$ complex shows undistinguishable gating properties to the full-length $Ca_V2.2$, in terms of voltage-dependent activation and steady-state inactivation (Fig. 1a-1b; Extended Data Fig. 1a-1b). Thus, the $Ca_V2.2^{EM}$ construct was subjected to further structural and functional

studies. The purified $Ca_V2.2^{EM}$-α2δ1-β1 complex ($Ca_V2.2$ complex) displaying monodisperse peak on both SEC and SDS-PAGE further confirmed that all three subunits were present in the complex sample (Extended Data Fig. 1c-1d).

To elucidate its architecture, we carried out cryo-EM study of the $Ca_V2.2$ complex and obtained the final reconstruction at 2.8 Å resolution for the $Ca_V2.2$ complex (Fig. 1c, Extended Data Fig. 2 and Extended Data Table 1). Cryo-EM map of the $Ca_V2.2$ is rich of structural features, including densities for side chains, N-glycans, disulfide bonds, and associated lipid molecules, which enabled us to unambiguously de novo build atomic models of the $Ca_V2.2$ complex (Fig. 1d and Extended Data Fig. 2e). Of approximately 118 Å × 113 Å × 169 Å in sizes, the structure of the $Ca_V2.2$ complex contains α, α2δ1, and β1 subunits, and closely resembles the classic shape of $Ca_V1.1$.

The α-subunit is composed of four transmembrane domains, D_I–D_{IV}, which form an ion conducting pore in a domain swapped fashion. Each domain is composed of six helices (S1–S6), of which S1–S4 helices form the voltage sensing domain (VSD). Four VSDs (VSD_I–VSD_{IV}) encircle the central pore formed by S5 and S6 helices from all four domains. The β1 subunit comprises a Src homology 3 (SH3) domain and a guanylate kinase (GK) domain. The GK domain, through its alpha-interacting domain (AID) helix, interacts with the $Ca_V2.2$ (i.e., the α-subunit). Nevertheless, the GK domain was not well resolved in our cryo-EM map, presumably due to conformational heterogeneity (Fig. 1c-1d). The α2δ1 subunit is divided into α2 and δ subunits, which are linked by a disulfide bond (C404-C1059) and associate with the α-subunit by interacting with extracellular loops (ECLs, in particular the loops between S5 and S6 helices) ECL_I, ECL_{II}, ECL_{III}, and the S1–S2 loop from VSD_I. The structure of human α2δ1 in our complex is nearly identical with rabbit α2δ1 resolved in the $Ca_V1.1$ complex, with root-mean-square-deviation (r.m.s.d.) of ~1.1 Å.

Ion conduction pore of the $Ca_V2.2$ complex

The central pore is made up of helices S5 and S6 from all four domains of the α-subunit (Fig. 2a-2b). In each domain, a re-entrant P-loop is located between the S5 and S6 helices and contains two short helices, P1 and P2, connected by a short linker. Four P-loops form a funnel-like shape and line the outer entry to the pore. Four highly conserved glutamate

residues, E^{314}, E^{663}, E^{1365}, and E^{1655}, form a selectivity-filter ring at the bottom of the funnel, which is one of the narrowest segments of the central pore (Fig. 2c). These four acidic residues, together with surrounding negatively charged residues, create a strong negative electric field strength to attract cations and repel anions. This pore region also functions as a selectivity filter to discriminate Ca^{2+} from other cation ions. We did identify a strong density within the selectivity filter and close to the glutamate cluster (Fig. 2d-2e). Presumably, this piece of density represents a calcium ion, consistent with observations in previous structures of Ca_V channels [12-16]. Thus, on the extracellular side, the S5, S6 helices as well as the P-loops contribute to the formation and stability of the selectivity filter.

On the intracellular side, the pore-lining S6 helices comprise an intracellular gate to control ion permeation (Fig. 2f). The $Ca_V2.2$ complex was determined in the absence of membrane potential, and thus is likely to represent a depolarization state. The cytoplasmic ends of the S6 helices are converged and form a hydrophobic seal through a cluster of hydrophobic residues (Fig. 2f). In each of the four domains, the S5 helix is positioned proximal to the S6 helix and connects to S4 of VSD through an amphipathic horizontal helix (termed S4-S5 helix, approx. 16 residues). This S4-S5 helix interacts with the S6 helix, and thus couples S4 movement in responding to depolarization of membrane potential with gate opening.

The central pore of the $Ca_V2.2$ channel is further compared with those from the $Ca_V1.1$ (PDB ID: 5GJW), and $Ca_V3.1$ (PDB ID: 6KZP) channels. The S5-S6 ECLs exhibit nontrivial conformational discrepancy among these structures (Extended Data Fig. 3a, 3b, 3d and 3e). The $Ca_V2.2$ α-subunit possesses shorter ECL_I, ECL_{II}, and ECL_{III}, but this structural difference does not hamper binding of the $\alpha2\delta1$ subunit. The S1-S2 loops of VSD_{II}, also involved in interactions with the $\alpha2\delta1$ subunit, are nearly identical in both $Ca_V2.2$ and $Ca_V1.1$. Therefore, the $\alpha2\delta1$ subunits in both $Ca_V2.2$ and $Ca_V1.1$ complexes display similar binding geometry. In contrast, the ECLs of the $Ca_V3.1$ channel exhibit remarkable structural discrepancy from the corresponding loops of $Ca_V1.1$ and $Ca_V2.2$, thus giving rise to incompatibility of the $\alpha2\delta1$ subunit with $Ca_V3.1$ (Extended Data Fig. 3b and 3e). Despite of these structural differences occurring at ECLs, the transmembrane helices S5, S6 as well as the selectivity filter of $Ca_V2.2$ are superimposable with $Ca_V1.1$ and $Ca_V3.1$, yielding

r.m.s.d of ~1.8 Å for $Ca_V1.1$ (for 332 C_α atom-pairs), and ~1.6 Å for $Ca_V3.1$ (for 300 C_α atom-pairs), respectively (Extended Data Fig. 3c and 3f). In particular, the intracellular gate formed by the four helix-bundle of S6 helices is nearly identical in all three structures, assuming a closed form (Extended Data Fig. 3g). The $S6_{II}$ helix of the $Ca_V2.2$ extends into the cytoplasmic, and is longer than that of the $Ca_V1.1$. Consequently, C-terminus of the $S6_{II}$ helix forms a close contact with the $\beta 1$ subunit in the $Ca_V2.2$ complex, which is not observed in the structure of $Ca_V1.1$. Furthermore, the cytoplasmic part of the S6 helix bends by 13° compared with that in $Ca_V1.1$ (Extended Data Fig. 3h), which may affect gate opening and represent a potential regulatory mechanism of the β subunit.

Voltage sensor of the N-type Ca_V channel

A hallmark feature of the Ca_V channel is to open or close the channel in respond to variation of the membrane potential. Surrounding the central pore, the four VSDs play essential roles in converting the electrostatic signal into conformational change of the intracellular gate. Each VSD is composed of S1–S4 transmembrane helices. Each S4 helix contains several positively charged residues, either arginine or lysine, spaced at intervals of three. $Ca_V2.2$ is a depolarization-activated channel. Upon depolarization of the membrane potential, the gating charges on the S4 helix move toward the extracellular cavity of the VSD. The two cavities are separated by a highly conserved hydrophobic constriction site. When the gating charges pass through this hydrophobic seal, existing interactions of the gating charges with hydrophilic and negatively charged residues on surrounding helices are disrupted on one side, and new interactions are formed on the other side. The displacement of the S4 helices across the electrostatic field of the membrane potential would induce lateral movement of the S4-S5 linkers, resulting in disengagement between S5 and S6 helices and thus the channel opening.

In our structure, the S4 helices adopt 3_{10}-helix conformation, which is consistent with observations from previous structures of voltage-gated ion channel, including Ca_V and Na_V channels, allowing the side chains of gating-charge residues to be aligned on the same side of the helix surface. Using the central pore as a reference, superimposition of the structure of $Ca_V2.2$ onto that of $Ca_V1.1$ shows fairly superimposable VSD_I, VSD_{III}, and VSD_{IV},

demonstrating that they are stabilized in the same, presumably activated state (Extended Data Fig. 4a-4e). In contrast, VSD_{II} of $Ca_V2.2$ exhibits discernable conformational rearrangement compared with that from the $Ca_V1.1$ structure. Taking a closer look at the four VSDs, we found that four, four, and three gating charges are located at the extracellular aqueous cavities of VSD_I, VSD_{III}, and VSD_{IV}, respectively, and interact with polar residues residing on nearby S1-S3 helices, consistent with observations from the available structures of Ca_V channels [12-14,16] (Figs. 3a, 3c, 3d; Extended Data Figs. 4c-4e). Strikingly, in VSD_{II} only one arginine (R578) on the S4 helix is located on the extracellular side of the hydrophobic seal, but the other four conserved gating charges (R581, R584, K587, and K590) are located in the intracellular cavity, indicating that VSD_{II} is stabilized at the resting state. Among the basic residues, K590 is located at a position where S4 becomes unwound, and is completely exposed to the solvent (Fig. 3b). The asymmetric activation of $Ca_V2.2$ VSDs suggests that individual VSD may sense membrane potential asynchronously, which is reported to be important for eukaryotic Na_V activation and inactivation [26].

To investigate conformational change of the VSD_{II} of $Ca_V2.2$ upon depolarization, we overlaid its structure at the resting state (VSD_{II}^R) onto that of $Ca_V1.1$ at the activated state (VSD_{II}^A), and found that these VSD_{II} structures are highly superimposable in helices S1, S2, and S3 (Fig. 3e-3f). In contrast, the S4 helix slides to the intracellular side in the resting state. Consequently, extracellular halves of S3 helix bends ~15° toward S4 in the resting state (Fig. 3e). Using the S5 and S6 helices as a superimposition reference, the VSD_{II} undergoes substantial conformational change relative to the central pore between these two states. In particular, in transition from activated state to the resting state, the cytoplasmic sides of both S1 and S2 helices in $Ca_V2.2$ rotate toward the central pore (Fig. 3g). Consequently, the intracellular and extracellular terminus of the S3 helices are remarkably displaced approaching to the central pore by 4 Å and 9 Å, respectively. In addition to inwardly sliding, the S4 helices also slightly shift toward the pore domain (Fig. 3h). Interestingly, even though distinguishable conformational change occurs in VSD_{II}, the extracellular end of the S1-S2 helix hairpin forms similar interactions with helices S5 and P1 from domain III. It appears that this interaction is stabilized by a cholesterol derivative cholesteryl hemisuccinate (CHS), which is determined in both our structure of $Ca_V2.2$ and

the structure of $Ca_V3.1$ (Extended Data Fig. 4f), consistent with earlier reports suggesting that cholesterol is important to regulating activity of Ca_V channels [27,28].

Compared with S4 in the activated VSD_{II} from $Ca_V1.1$, the S4 helix in the resting state undergoes a sliding movement by two helical-turns, ~13 Å, towards intracellular side (Fig. 3h). The displacement of S4 is comparable with previous observations in structures of TPC1 channel and Na_VAb channel (Extended Data Fig. 4h-4i) [29-31]. Except R5 (K590) of $Ca_V2.2$, all gating charges are facing to one side, and no rotation about the helix axis is observed, which support a sliding-helix model of voltage-dependent gating [31,32]. As a consequence of the S4 inwardly sliding, the S4-S5 linker tilted by 11° degree towards intracellular side, and this movement generates more contacts between the S4-S5 linker and S6 helix, and thus stabilize the inner gate at its closed state.

An extra density was identified laying above the S4-S5 linker of domain II in the cryo-EM map, which presumably represents a lipid with two hydrophobic tails and a 'palm'-like head group. Its head group is located at the intracellular cavity of the VSD_{II} and flanked by S3 and S4 helices (Fig. 3i). Its hydrophobic tails project toward the extracellular side of the membrane (Extended Data Fig. 5a). This lipid appears to act as a plug and would block the S4 helix from upwardly sliding, reminiscent of the PIP_2 that attenuates opening of the $K_V1.2$ channel by interacting with the S4-S5 linker [33]. We attempted to fit a PIP_2 into the density. Whereas its hydrophobic tails and inositol ring agree well with the density, the two phosphate groups attached to the inositol ring could not be well resolved (Extended Data Fig. 5a). Considering the PIP_2 is predominant in the inner-leaflet of the plasma membrane and reported to left shift the activation curve of $Ca_V2.2$, which are consistent with our structural observations, we postulate that this lipid molecule is a PIP_2. However, PIP_2 molecule was not robustly detected using lipid blot and mass spectrometry methods due to poor yield of the $Ca_V2.2$ complex. In a closer look at the PIP_2-like lipid binding site, several positively charged residues from helices S0, S4, and S4-S5 linker provide a highly positively charged environment for PIP_2 binding (Extended Data Fig. 5b-5c). Similar local environment is not observed in the other three VSDs (Extended Data Fig. 5b), implying a mechanism by which PIP_2 selectively binds with VSD_{II}. In addition, the putative inositol ring of PIP_2 is positioned proximal to the AID helix of the β1 subunit, and this observation is consistent with

previous investigations indicating that regulation role of PIP_2 on the Ca_V channel depends on types of β subunits [34].

Inactivation mechanism of the Ca_V2 channels

The N-type Ca_V channel bears a preferential voltage-dependent closed-state inactivation (CSI) [17,18], featuring Ca^{2+} insensitive U-shaped inactivation curve, substantial inactivation accumulated during interpulse in a two-pulse protocol and cumulative inactivation during voltage-clamped action potential trains [17]. In our structure, the intracellular gate is comparable with that in structures of the $Ca_V1.1$ and $Ca_V3.1$, and appears to be stabilized at a closed state (Extended Data Fig. 3g). Strikingly, an additional α-helix was unexpectedly determined underneath the intracellular gate and flanked by the four S6-helix bundle, forming a 36° angle to the membrane plane (Fig. 4a), and has not been observed in previous structures of Ca_V channels. The high resolution cryo-EM map aided us to register the amino-acid sequence to the model. This helix is composed of residues range from A764 to S783, which belongs to the DII-III linker (Fig. 4b). The side chain of W768 points upward into the intracellular gate, forms extensive hydrophobic interactions with residues from S6 helices (Fig. 4b-4c), and thus stabilizes the intracellular gate at its closed state. Thus, we term this 6-turn helix as W-helix. In addition to the tryptophan as a plug inserting into and blocking the intracellular gate, the other residues from the W-helix extensively interact with the S6 helices, including hydrogen-bond and electrostatic interaction, to further strengthen the association of the W-helix with the intracellular gate (Fig. 4b-4c). We speculate that the freshly uncovered W-helix functions as the channel-blocking ball of the “ball-and-chain” model and is important for the stability of the intracellular gate in the closed state, thus contributing to the close-state inactivation of the $Ca_V2.2$.

To investigate the functional role of the W-helix and to validate our hypothesis, we designed two mutants, including deletion of the W-helix ($Ca_V2.2^{\Delta W\text{-}Helix}$) and a point-mutation variant W768Q ($Ca_V2.2^{W768Q}$), and performed whole-cell patch clamp recording experiment, with Ba^{2+} as charge carriers. The voltage activation curves of these two mutants were indistinguishable with the WT $Ca_V2.2$ complex, suggesting the W-helix might not participate

in channel activation. In sharp contrast, the steady-state inactivation curves of these two variants exhibit a depolarizing shift of ~24 mV (Fig. 4d and Extended Data Fig. 6a-6b), indicating the W-helix and W768 are critical for the CSI. To investigate recovery properties of the CSI, the membrane potential of pre-pulse was held at -40mV, where the channel has not been opened yet. It turns out the recovery of the $Ca_V2.2^{\Delta W\text{-Helix}}$ variant is significantly faster than that of WT complex (Fig. 4e and Extended Data Fig. 6c), which further support that the W-helix plays vital roles in CSI of $Ca_V2.2$ channel. These results are also in line with a previous functional characterization showing that domain II–III linker is crucial for CSI of $Ca_V2.2$ [19,35]. To further validate our finding in a more physiologically relevant condition, we repetitively activated the $Ca_V2.2$ channels with action potential (AP) trains which were recorded in hippocampal CA1 neurons in whole-cell current-clamp configuration. As observed in previous reports [17,19], we found that WT $Ca_V2.2$ channels exhibited cumulative inactivation in response to AP trains (Fig. 4f and Extended Data Fig. 6d). Interestingly, $Ca_V2.2^{\Delta W\text{-Helix}}$ variant inactivated more slowly during the AP train, suggesting that W-helix-regulated close-state inactivation contributed to $Ca_V2.2$ channel inactivation during the AP trains, thus may play an important role in short-term synaptic plasticity [36]. Collectively, W-helix is manifested to be essential for CSI of the $Ca_V2.2$ channel. Interestingly, the W-helix is only conserved in the Ca_V2 subfamily (Extended Data Fig. 7), suggesting that P/Q-type and R-type Ca_V channels may adopt the same inactivation mechanism.

Method

Whole-cell Voltage-clamp recordings of $Ca_V2.2$ channels in HEK 293T Cells

HEK 293T cells were cultured with Dulbecco's Modified Eagle Medium (DMEM) (Gibco) added 15% (v/v) fetal bovine serum (FBS) (PAN-Biotech) at 37°C with 5% CO2. The cells were grown in the culture dishes (d = 3.5 cm) (Thermo Fisher Scientific) for 24 h and then transiently transfected with 2 μg control or mutant plasmids containing human N-type calcium channel isoform α1B, β1, $\alpha2\delta$1 and GFP using 1.5 μg Lipofectamine 2000 Reagent (Thermo Fisher Scientific). Experiments were performed 12 to 24 hours post transfection at room temperature (21 ~ 25°C) as described previously [37]. In brief, cells were placed on a

glass chamber containing 105 mM NaCl, 10 mM $BaCl_2$, 10 mM HEPES, 10 mM D-Glucose, 30 mM TEA-Cl, 1 mM $MgCl_2$, 5 mM CsCl, (pH = 7.3 with NaOH and osmolarity of ~310 $mosmol^{-1}$). Whole-cell voltage-clamp recordings were made from isolated, GFP-positive cells using 1.5 ~ 2.5 MΩ fire polished pipettes (Sutter Instrument) when filled with standard internal solution, containing 135 mM K-Gluconate, 10 mM HEPES, 5 mM EGTA, 2 mM $MgCl_2$, 5 mM NaCl, 4 mM Mg-ATP, (pH = 7.2 with CsOH and osmolarity of ~295 $mosmol^{-1}$). Whole-cell currents were recorded using an EPC-10 amplifier (HEKA Electronic) at 20 kHz sample rate and was low pass filtered at 5 kHz. The series resistance was 2 ~ 4.5 MΩ and was compensated 80 ~ 90%. The data was acquired by PatchMaster program (HEKA Electronic).

To characterize the activation properties of $Ca_V2.2$ channels, cells were held at −100 mV and then a series of 200ms voltage steps from −60 mV to +50 mV in 5 mV increments were applied. The inactivation properties of $Ca_V2.2$ channels were assessed with a 10s holding-voltages ranging from −100 mV to −15 mV (5 mV increments) followed by a 135 ms test pulse at +10 mV. To assess the time-dependent recovery from close-state inactivation, cells were depolarized to −40 mV (pre-pulse) for 200 ms to inactivate the $Ca_V2.2$ channels, and a recovery hyperpolarization steps to −100 mV were applied for the indicated period (4 ms ~ 512 ms), followed by a 35 ms test pulse at +10 mV. To analysis the persistent inactivation of $Ca_V2.2$ channels following action potential trains, the cells were held at −100 mV and then a physiologically relevant AP train was applied. The AP train used to repetitively activate $Ca_V2.2$ channels was obtained from a hippocampal CA1 pyramidal neuron in whole-cell current-clamp mode [38]. The spike pattern contains 13 action potentials in 2 seconds (mean frequency 6.5 Hz). The percentage inactivation of $Ca_V2.2$ channels was calculated from the first spike eliciting maximal current to the other spikes in the AP trains.

All data reported as mean ± SEM. Data analyses were performed using Origin 2019b (Origin Lab Corporation), Excel 2016 (Microsoft), GraphPad Prism 6 (GraphPad Software, Inc.) and Adobe illustrator 2018 (Adobe Systems Incorporated). Steady-state activation curves were generated using a Boltzmann equation.

$$\frac{g}{g_{max}} = \frac{1}{1 + \exp(V - V_{0.5})/k}$$

Where g is the conductance, g_{max} is the maximal conductance of $Ca_V2.2$ during test pulse, V is the test potential, $V_{0.5}$ is the half-maximal activation potential and k is the slope factor.

Steady-state inactivation curves were generated using a Boltzmann equation.

$$\frac{I}{I_{max}} = \frac{1}{1 + \exp(V - V_{0.5})/k}$$

Where I is the current at indicated test pulse, I_{max} is the maximal current of $Ca_V2.2$ activation during test-pulse, V is the test potential, $V_{0.5}$ is the half-maximal inactivation potential and k is the slope factor.

Recovery curves from close-state inactivation were the results from seven to nine independent experiments where series of recovery traces from inactivation time points were acquired. The data were fit using a single exponential of the following equation.

$$\frac{I}{I_{max}} = (y_0 - 1) * \exp\left(-\frac{t}{\tau}\right) + 1$$

Where I is the current at indicated time delay, I_{max} is the current at 512 ms of time delay, y_0 is the non-inactivated current at −40mV of pre-pulse, t is the time (the delay between pre-pulse and test-pulse) and τ is the time constant of recovery from close-state inactivation. Statistical significance ($P < 0.05$) was determined using unpaired Student's t-tests or one-way ANOVA with Tukey's post hoc test.

Expression and purification of human $Ca_V2.2$-α2δ1-β1 complex

The DNA fragments of human $Ca_V2.2$ (UniProtKB accession: Q00975), α2δ1 (UniProtKB accession: P54289) and β1 (UniProtKB accession: Q02641) were amplified from a human cDNA library. The $Ca_V2.2$ (full-length wide-type or N-terminal 64-residue truncated), α2δ1 and β1 subunits were subcloned into a modified pEG BacMam vector. A superfolder GFP (sfGFP) and a Twin-Strep tag were tandemly attached at the C-terminus of the $Ca_V2.2$ for monitoring protein expression and affinity purification, respectively. The components of $Ca_V2.2$ complex were co-expressed in HEK 293F cells using the Bac-to-Bac baculovirus expression system. P1 and P2 viruses of each subunits were obtained using Sf9 insect cells. The P2 viruses were used to infect HEK 293F cells supplemented with 1% (v/v) fetal bovine serum when the cells density reached 2.5×10^6 cells/mL. The infected

HEK 293F cells were cultured at 37°C in suspension and 5% CO_2 in a shaking incubator. 10 mM sodium butyrate was added after 12 hours. The cells were harvested after 48 hours and were stored at −80°C immediately after being frozen in liquid nitrogen.

Cells expressing $Ca_V2.2$ complex were resuspended and broken in a purification buffer (20 mM HEPES pH 7.5, 150 mM NaCl, 5 mM β-mercaptoethanol (β-ME), aprotinin (2 μg/mL), leupeptin (1.4 μg/mL), pepstatin A (0.5 μg/mL)) using a Dounce homogenizer. Subsequently, the membranes were collected by centrifugation at 100,000 × g for 1 h and solubilized in the solubilization buffer (20 mM HEPES pH 7.5, 150 mM NaCl, 5 mM β-mercaptoethanol (β-ME), 1% (w/v) n-Dodecyl β-D-maltoside (DDM, Anatrace), 0.2% (w/v) cholesteryl hemisuccinate (CHS, Anatrace)) at 4°C for 2 h with rotation. The insoluble cell debris was removed by centrifugation at 100,000 × g for 1 h. The resulting supernatant was collected and passed through 2 mL Streptactin Beads, which was pre-equilibrated with the wash buffer (20 mM HEPES pH 7.5, 150 mM NaCl, 5 mM β-ME and 0.03% (w/v) glyco-diosgenin (GDN, Anatrace)) and washed with 10 column volumes of wash buffer supplemented with 2 mM ATP and 5 mM $MgCl_2$. The $Ca_V2.2$ complex was eluted with the wash buffer supplemented with 5 mM desthiobiotin and 1 mM $CaCl_2$, and then concentrated in the 100 kDa MW cut-off spin concentrators (Merck Millipore, Germany). For further purification, the concentrated protein sample was subjected to a Superose 6 Increase 10/300 GL gel filtration column (GE Healthcare, USA) pre-equilibrated in the wash buffer supplemented with 1 mM $CaCl_2$. The peak fractions between 11.5 mL and 13.5 mL were pooled and concentrated to about 1.8 mg/mL for cryo-EM sample preparation.

Cryo-EM sample preparation and data collection

A droplet of 2.5 μL of purified $Ca_V2.2$ complex was applied on the Quantifoil 1.2-1.3 Au 300 mesh grids glow-discharged for 60 s under H_2-O_2. The grids were then blotted for 4-5 s at 4°C under condition of 100% humidity and vitrified in liquid ethane using a Vitrobot Mark IV.

Cryo-EM data were collected on a 300-kV microscope using a K2 Summit direct electron detector and a GIF Quantum LS energy filter. The slit was set to 20 eV. Movie stacks were acquired at a calibrated magnification of 105,000× in the super-resolution

mode, with defocus values ranging from −1.2 to −2.2 μm. The pixel size on motion-corrected micrographs was 1.04 Å. The micrographs were collected under a dose rate of ~9.6 $e^-/(Å^2s)$ and dose-fractioned in 32 frames, yielding a total accumulated dose of ~60 $e^-/Å^2$.

Data Processing

A total of 2,300 micrographs were motion-corrected and dose-weighted using MotionCor2 with 5 × 5 patches[39], followed by CTF estimation using GCTF[40] and particle picking using both blob picker and template picker in cryoSPARC[41]. Several rounds of 2D and 3D classifications were performed in RELION to remove junk particles [42]. Initial multi-reference 3D classification generated 6 classes. The class 5 accounts for 26.1% of total particles, displaying discernible structural features, including the secondary structure elements of the α, β1 and α2δ1 subunits. This class were selected and subjected to another round of 3D classification, giving rise to two classes with visible and continuous transmembrane helices. The particles from these two new classes were subjected to 3D refinement, generating a 3.5-Å resolution map. Subsequently, one more round of 3D classification was performed without further particle alignment. Two of the most populated classes were used for further 3D refinement, Bayesian polishing, and CTF refinement in RELION. The particles were then imported into cryoSPARC and subjected to Non-uniform Refinement. The final map was reported at 2.8-Å resolution according to golden standard *Fourier* shell correlation (GSFSC) criterion.

Model building

The cryo-EM map of $Ca_V2.2$ complex showed clear densities for most side chains and N-glycans, which allowed us to reliably build and adjust the model. The homology models of α and α2δ1 subunits were extracted from the structures of *O. cuniculus* $Ca_V1.1$ complex (PDB IDs: 5GJW[43] and 7JPX[44]). The homology models of β subunits were extracted from the structures of *R. norvegicus* $Ca_V\beta_{2\alpha}$ (PDB ID: 1T0J [45]). All of these homology models were fitted into the cryo-EM map as rigid bodies using the UCSF Chimera [46]. The resulting model was then manually inspected and adjusted in COOT [47], followed by refinement

against the cryo-EM map in real space using the phenix.real_space_refine utility. The model stereochemistry was evaluated using the Comprehensive validation (cryo-EM) utility in the PHENIX software package [48].

All figures were prepared with ChimeraX or PyMOL (Schrödinger, LLC) [49,50].

Data availability

The three-dimensional cryo-EM density maps of the $Ca_V2.2$ complex have been deposited in the Electron Microscopy Data Bank under the accession code EMD-xxxx. The coordinates for the $Ca_V2.2$ complex have been deposited in Protein Data Bank under accession code xxxx.

Author contribution

Y.Z. and D.J. conceived the project. Y.D. carried out molecular cloning and cell biology experiments. Y.D., Y.W., Y.L. and B.Y. expressed, purified protein complex sample and prepared sample for cryo-EM study. Y.D., Y.G. and Y.W. carried out cryo-EM data collection. Y.G. Z.Y.Y. and Y.Z. processed the cryo-EM data and prepared figures. Y.W. and B.L. built and refined the atomic model. Z.H. and Y.Z. designed and S.X. performed electrophysiological experiments. X.C.Z., D.J. and Y.Z. analyzed the structure. Y.Z. prepared initial draft of the manuscript. X.C.Z., D.J., Z.H. and Y.Z. edited the manuscript with input from all authors in the final version.

Acknowledgments

We thank X. Huang, B. Zhu, X. Li, L. Chen, and other staff members at the Center for Biological Imaging (CBI), Core Facilities for Protein Science at the Institute of Biophysics, Chinese Academy of Science (IBP, CAS) for the support in cryo-EM data collection. We thank Yan Wu for his research assistant service. This work is funded by Chinese Academy of Sciences Strategic Priority Research Program (Grant XDB37030304 to Y.Z. and Grant XDB37030301 to X.C.Z), the National Natural Science Foundation of China (31971134 to X.C.Z., 81371432 to Z.H.) and Institute of Physics, Chinese Academy of Sciences

(E0VK101 to D.J.).

Conflict of interest

All authors declare that there is no conflict of interest that could be perceived as prejudicing the impartiality of the research reported.

Reference

1 Reuter, H. Properties of two inward membrane currents in the heart. *Annual review of physiology* **41**, 413-424 (1979).

2 Catterall, W. A. Excitation-contraction coupling in vertebrate skeletal muscle: a tale of two calcium channels. *Cell* **64**, 871-874, doi:10.1016/0092-8674(91)90309-m (1991).

3 Tsien, R. W., Lipscombe, D., Madison, D. V., Bley, K. R. & Fox, A. P. Multiple types of neuronal calcium channels and their selective modulation. *Trends Neurosci* **11**, 431-438, doi:10.1016/0166-2236(88)90194-4 (1988).

4 Catterall, W. A. & Few, A. P. Calcium channel regulation and presynaptic plasticity. *Neuron* **59**, 882-901, doi:10.1016/j.neuron.2008.09.005 (2008).

5 Nowycky, M. C., Fox, A. P. & Tsien, R. W. Three types of neuronal calcium channel with different calcium agonist sensitivity. *Nature* **316**, 440-443 (1985).

6 Snutch, T. P. & Reiner, P. B. Ca2+ channels: diversity of form and function. *Current opinion in neurobiology* **2**, 247-253 (1992).

7 Catterall, W. A., Perez-Reyes, E., Snutch, T. P. & Striessnig, J. International Union of Pharmacology. XLVIII. Nomenclature and structure-function relationships of voltage-gated calcium channels. *Pharmacological reviews* **57**, 411-425 (2005).

8 Olivera, B. M., Miljanich, G. P., Ramachandran, J. & Adams, M. E. Calcium channel diversity and neurotransmitter release: the ω-conotoxins and ω-agatoxins. *Annual review of biochemistry* **63**, 823-867 (1994).

9 Westenbroek, R. E. *et al.* Biochemical properties and subcellular distribution of an N-type calcium channel alpha 1 subunit. *Neuron* **9**, 1099-1115, doi:10.1016/0896-6273(92)90069-p (1992).

10 Westenbroek, R. E., Hoskins, L. & Catterall, W. A. Localization of Ca2+ channel subtypes on rat spinal motor neurons, interneurons, and nerve terminals. *J Neurosci* **18**, 6319-6330, doi:10.1523/jneurosci.18-16-06319.1998 (1998).

11 Weiss, N. The first disease connection for Cav2.2 channels. *Gen Physiol Biophys* **34**, 217-219, doi:10.4149/gpb_2015014 (2015).

12 Wu, J. *et al.* Structure of the voltage-gated calcium channel Cav1. 1 complex. *Science* **350** (2015).

13 Wu, J. *et al.* Structure of the voltage-gated calcium channel Ca v 1.1 at 3.6 Å resolution. *Nature* **537**, 191-196 (2016).

14 Zhao, Y. *et al.* Molecular basis for ligand modulation of a mammalian voltage-gated Ca2+ channel. *Cell* **177**, 1495-1506. e1412 (2019).

15 Gao, S. & Yan, N. Structural Basis of the Modulation of the Voltage-Gated Calcium Ion Channel Cav1. 1 by Dihydropyridine Compounds. *Angewandte Chemie* **133**, 3168-3174 (2021).

16 Zhao, Y. *et al.* Cryo-EM structures of apo and antagonist-bound human Ca v 3.1. *Nature* **576**, 492-497

(2019).

17 Patil, P. G., Brody, D. L. & Yue, D. T. Preferential closed-state inactivation of neuronal calcium channels. *Neuron* **20**, 1027-1038 (1998).

18 Jones, L. P., DeMaria, C. D. & Yue, D. T. N-type calcium channel inactivation probed by gating-current analysis. *Biophysical journal* **76**, 2530-2552 (1999).

19 Thaler, C., Gray, A. C. & Lipscombe, D. Cumulative inactivation of N-type CaV2. 2 calcium channels modified by alternative splicing. *Proceedings of the National Academy of Sciences* **101**, 5675-5679 (2004).

20 Suha, B.-C., Kima, D.-I., Falkenburgerb, B. H. & Hilleb, B. Membrane-localized β-subunits alter the PIP2 regulation of high-voltage activated Ca 2 channels. *PNAS* **109**, 3161-3166 (2012).

21 Vivas, O., Castro, H., Arenas, I., Elías-Viñas, D. & García, D. E. PIP2 hydrolysis is responsible for voltage independent inhibition of CaV2. 2 channels in sympathetic neurons. *Biochemical and biophysical research communications* **432**, 275-280 (2013).

22 Keum, D., Baek, C., Kim, D. I., Kweon, H. J. & Suh, B. C. Voltage-dependent regulation of CaV2.2 channels by Gq-coupled receptor is facilitated by membrane-localized β subunit. *J Gen Physiol* **144**, 297-309, doi:10.1085/jgp.201411245 (2014).

23 Hille, B., Dickson, E. J., Kruse, M., Vivas, O. & Suh, B.-C. Phosphoinositides regulate ion channels. *Biochimica et biophysica acta* **1851**, 844-856, doi:10.1016/j.bbalip.2014.09.010 (2015).

24 Wu, L., Bauer, C. S., Zhen, X.-g., Xie, C. & Yang, J. Dual regulation of voltage-gated calcium channels by PtdIns(4,5)P2. *Nature* **419**, 947-952, doi:10.1038/nature01118 (2002).

25 Rodríguez Menchaca, A., Adney, S., Zhou, L. & Logothetis, D. Dual Regulation of Voltage-Sensitive Ion Channels by PIP2. *Frontiers in Pharmacology* **3**, doi:10.3389/fphar.2012.00170 (2012).

26 Chanda, B. & Bezanilla, F. Tracking voltage-dependent conformational changes in skeletal muscle sodium channel during activation. *J Gen Physiol* **120**, 629-645, doi:10.1085/jgp.20028679 (2002).

27 Xia, F. *et al.* Inhibition of cholesterol biosynthesis impairs insulin secretion and voltage-gated calcium channel function in pancreatic beta-cells. *Endocrinology* **149**, 5136-5145, doi:10.1210/en.2008-0161 (2008).

28 Purcell, E. K., Liu, L., Thomas, P. V. & Duncan, R. K. Cholesterol influences voltage-gated calcium channels and BK-type potassium channels in auditory hair cells. *PloS one* **6**, e26289-e26289, doi:10.1371/journal.pone.0026289 (2011).

29 Guo, J. *et al.* Structure of the voltage-gated two-pore channel TPC1 from Arabidopsis thaliana. *Nature* **531**, 196-201 (2016).

30 Kintzer, A. F. & Stroud, R. M. Structure, inhibition and regulation of two-pore channel TPC1 from Arabidopsis thaliana. *Nature* **531**, 258-264 (2016).

31 Wisedchaisri, G. *et al.* Resting-State Structure and Gating Mechanism of a Voltage-Gated Sodium Channel. *Cell* **178**, 993-1003.e1012, doi:10.1016/j.cell.2019.06.031 (2019).

32 Zhang, X. C., Yang, H., Liu, Z. & Sun, F. Thermodynamics of voltage-gated ion channels. *Biophysics Reports* **4**, 300-319, doi:10.1007/s41048-018-0074-y (2018).

33 Rodriguez-Menchaca, A. A. *et al.* PIP₂ controls voltage-sensor movement and pore opening of Kv channels through the S4–S5 linker. *Proceedings of the National Academy of Sciences* **109**, E2399, doi:10.1073/pnas.1207901109 (2012).

34 Suh, B. C., Kim, D. I., Falkenburger, B. H. & Hille, B. Membrane-localized β-subunits alter the PIP2 regulation of high-voltage activated Ca2+ channels. *Proc Natl Acad Sci U S A* **109**, 3161-3166, doi:10.1073/pnas.1121434109 (2012).

35 Kaneko, S. *et al.* Identification and characterization of novel human Cav2. 2 (α1B) calcium channel variants lacking the synaptic protein interaction site. *Journal of Neuroscience* **22**, 82-92 (2002).

36 Catterall, W. A., Leal, K. & Nanou, E. Calcium channels and short-term synaptic plasticity. *The Journal of biological chemistry* **288**, 10742-10749, doi:10.1074/jbc.R112.411645 (2013).

37 McArthur, J. R. *et al.* Inhibition of human N- and T-type calcium channels by an ortho-phenoxyanilide derivative, MONIRO-1. *Br J Pharmacol* **175**, 2284-2295, doi:10.1111/bph.13910 (2018).

38 Liu, Y. *et al.* CDYL suppresses epileptogenesis in mice through repression of axonal Nav1.6 sodium channel expression. *Nature communications* **8**, 355, doi:10.1038/s41467-017-00368-z (2017).

39 Zheng, S. Q. *et al.* MotionCor2: anisotropic correction of beam-induced motion for improved cryo-electron microscopy. *Nature methods* **14**, 331-332 (2017).

40 Zhang, K. Gctf: Real-time CTF determination and correction. *Journal of structural biology* **193**, 1-12 (2016).

41 Punjani, A., Rubinstein, J. L., Fleet, D. J. & Brubaker, M. A. cryoSPARC: algorithms for rapid unsupervised cryo-EM structure determination. *Nature methods* **14**, 290-296 (2017).

42 Zivanov, J. *et al.* New tools for automated high-resolution cryo-EM structure determination in RELION-3. *elife* **7**, e42166 (2018).

43 Wu, J. *et al.* Structure of the voltage-gated calcium channel Ca(v)1.1 at 3.6 Å resolution. *Nature* **537**, 191-196, doi:10.1038/nature19321 (2016).

44 Madej, T. *et al.* MMDB and VAST+: tracking structural similarities between macromolecular complexes. *Nucleic acids research* **42**, D297-303, doi:10.1093/nar/gkt1208 (2014).

45 Van Petegem, F., Clark, K. A., Chatelain, F. C. & Minor, D. L., Jr. Structure of a complex between a voltage-gated calcium channel beta-subunit and an alpha-subunit domain. *Nature* **429**, 671-675, doi:10.1038/nature02588 (2004).

46 Pettersen, E. F. *et al.* UCSF Chimera—a visualization system for exploratory research and analysis. *Journal of computational chemistry* **25**, 1605-1612 (2004).

47 Emsley, P. & Cowtan, K. Coot: model-building tools for molecular graphics. *Acta crystallographica section D: biological crystallography* **60**, 2126-2132 (2004).

48 Adams, P. D. *et al.* PHENIX: a comprehensive Python-based system for macromolecular structure solution. *Acta Crystallographica Section D: Biological Crystallography* **66**, 213-221 (2010).

49 Goddard, T. D. *et al.* UCSF ChimeraX: Meeting modern challenges in visualization and analysis. *Protein Science* **27**, 14-25 (2018).

50 DeLano, W. L. Pymol: An open-source molecular graphics tool. *CCP4 Newsletter on protein crystallography* **40**, 82-92 (2002).

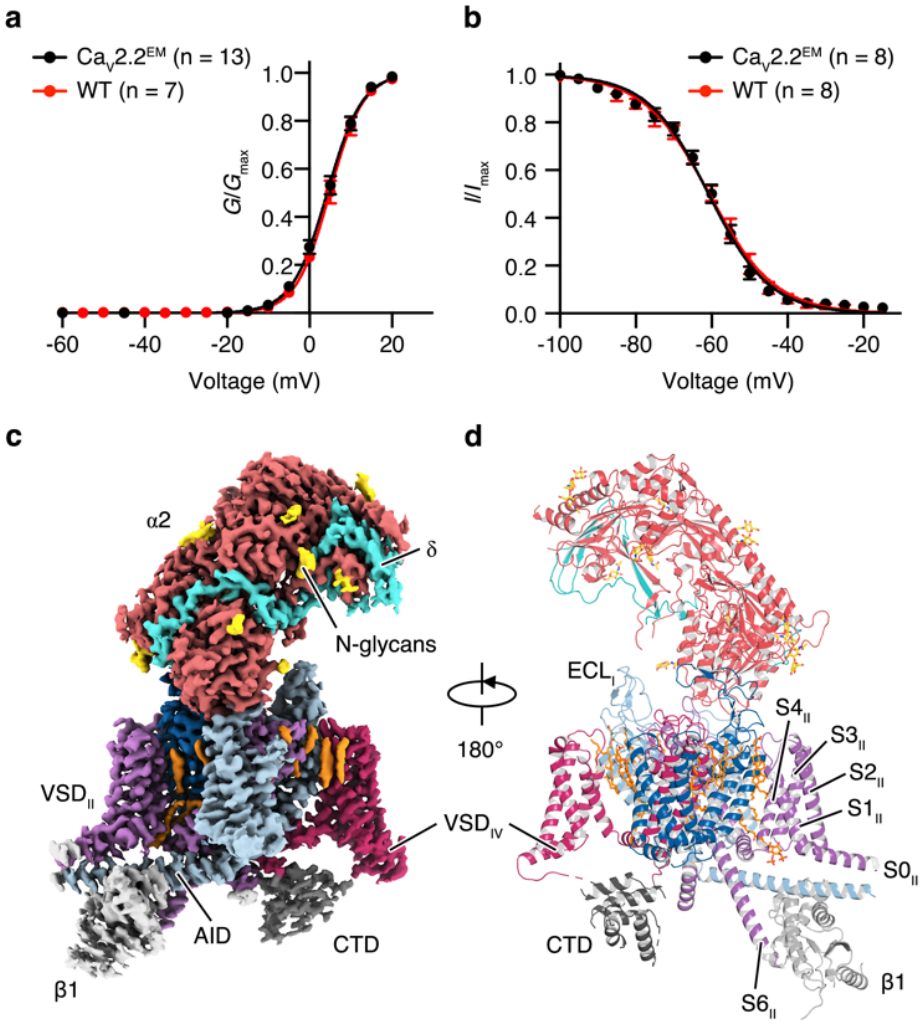

Figure 1. Architecture of the Ca$_V$2.2 complex.

a. Normalized conductance-voltage (*G*/*V*) relationship and the Boltzmann fits for the N-terminal truncated Ca$_V$2.2^{EM} complex and full-length wild type (WT) Ca$_V$2.2 complex. HEK 293T cells expressing the complex were stimulated with 200-ms depolarizing pulses between −60 mV and 50 mV in steps of 10 mV from a holding potential of −100 mV. **b**. Steady-state inactivation of the WT Ca$_V$2.2 complex and the Ca$_V$2.2^{EM} complex. Cells were stepped from a holding potential of −100 mV to pre-pulse potentials between −100 mV and -15 mV in 5 mV increments for 10 s. Black, Ca$_V$2.2^{EM} complex; red, full-length wild-type Ca$_V$2.2 complex. **c**–**d**. The density map and model of the Ca$_V$2.2^{EM} complex as seen in parallel to the membrane plane. The α2δ1 and β1 subunit, C-terminal domain (CTD), extracellular loops (ECL), alpha-interacting domain (AID), and transmembrane helices S1$_{II}$-S4$_{II}$ in VSD$_{II}$ were labeled. The α1 subunit is colored in light blue (D$_I$), violet (D$_{II}$), deep blue (D$_{III}$), magenta (D$_{IV}$), and grey (CTD) respectively. The β1, α2 and δ1 subunits are colored in light-grey, tomato-red, and turquoise, respectively. N-glycans is displayed and colored in gold.

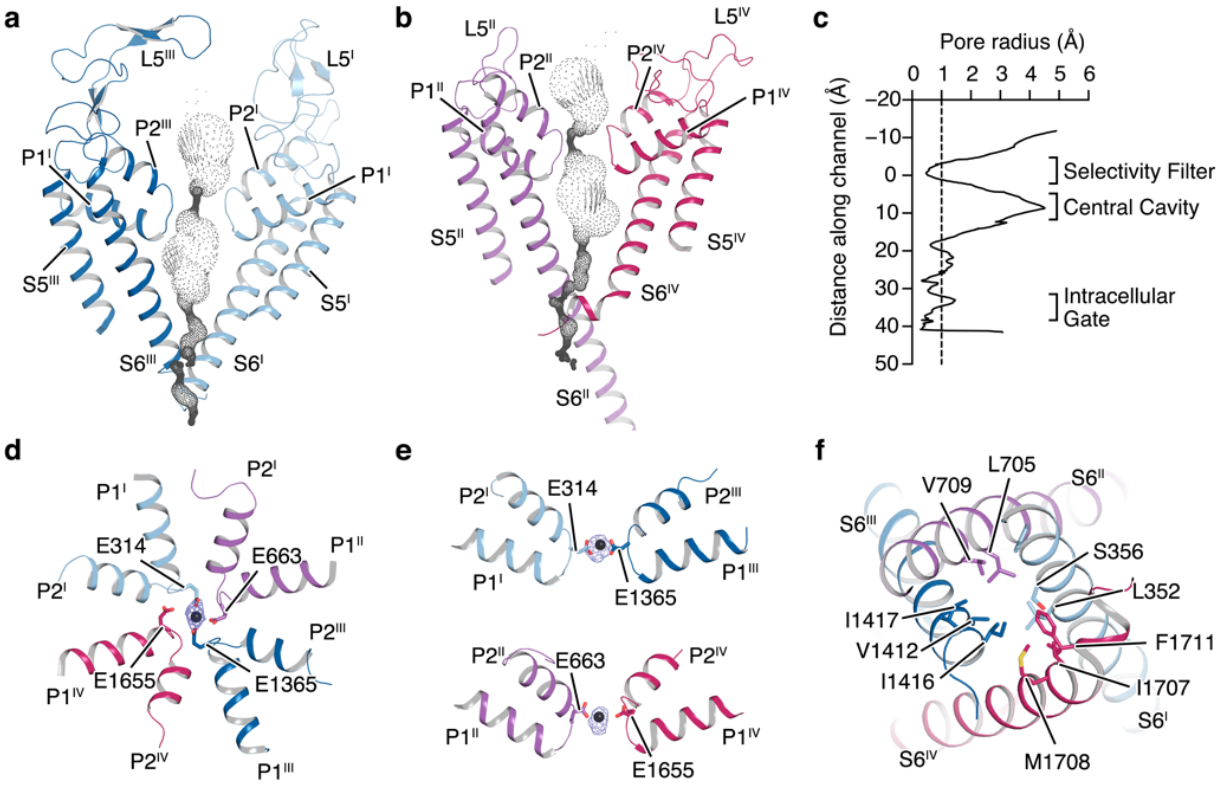

Figure 2. Ion conduction pore of the $Ca_V2.2$

a–**b**. Ion permeation pathways calculated by the program HOLE were shown in dots. The selectivity filter and S5-S6 helices are shown in cartoon and viewed in parallel to the membrane plane. **c**. Plot of pore radii for $Ca_V2.2$ complex. Vertical dashed line marks 1.0 Å pore radius. **d**–**e**. "Top-down" and side-view of the selectivity filter. The selectivity filter ring of four glutamate residues from the four domains of Ca_V channel were shown in sticks. A cation ion is shown as a grey sphere, overlaid with corresponding EM density colored in marine. **f.** The intracellular gate formed by four S6 helix viewed from intracellular side. Hydrophobic residues are shown in sticks. The segments from D_I, D_{II}, D_{III} and D_{IV} in the $Ca_V2.2$ complex are colored in light blue, violet, deep blue, and magenta, respectively.

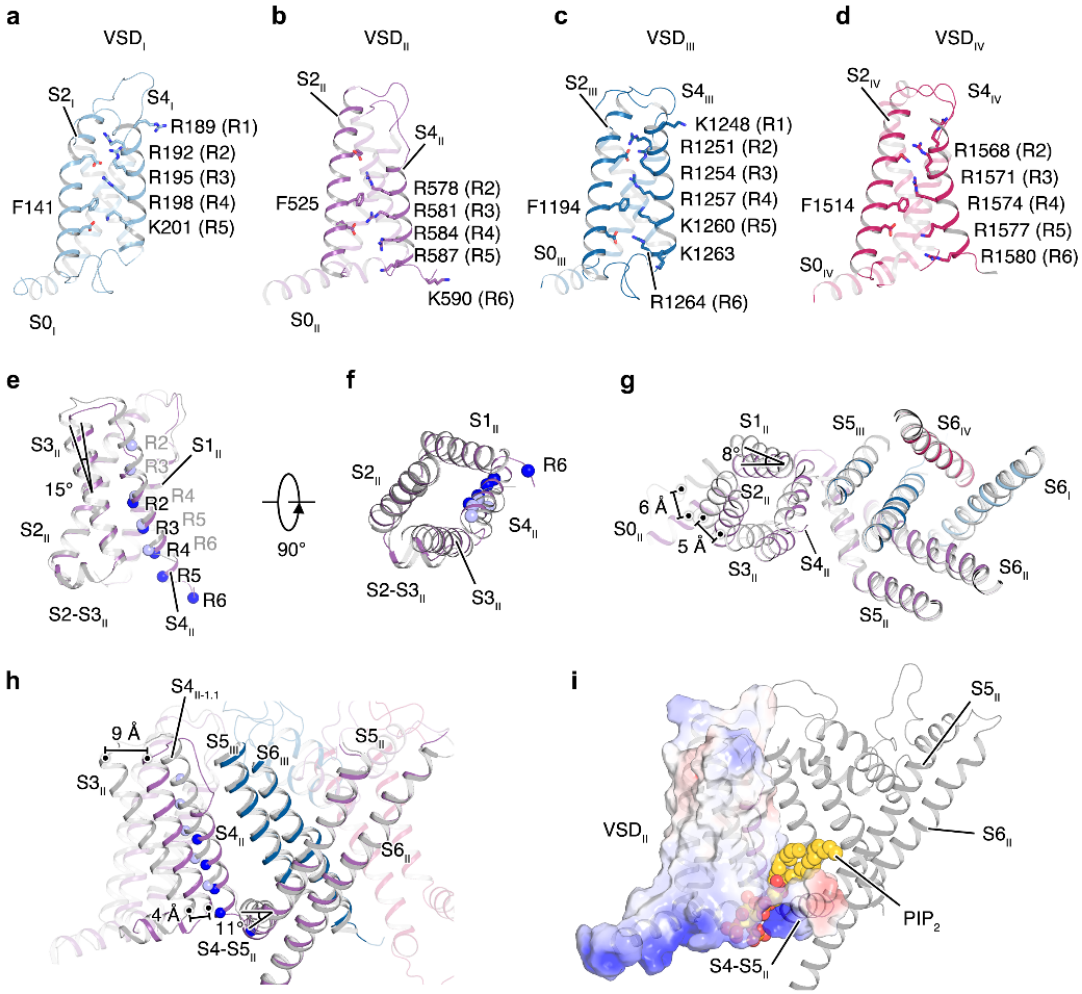

Figure 3. Structural analysis of the voltage-sensing domains.

a–**d**. Voltage sensing domains from D_I (**a**), D_{II} (**b**), D_{III} (**c**) and D_{IV} (**d**) are shown in cartoon. The gating-charge residues (R1-R6) on S4 helix and residues from surrounding helices are shown in sticks. **e**–**f**. Structural comparison of the VSD_{II} at resting state from $Ca_V2.2$ complex and activated state from $Ca_V1.1$ complex, viewed parallel (**e**) or perpendicular (**f**) to the membrane plane. The gating-charge residues are shown as spheres, colored in deep blue ($Ca_V2.2$) or light blue ($Ca_V1.1$). **g**–**h**. superimposition of the VSD_{II}^R and VSD_{II}^A using S5-S6 helices as a reference, viewed perpendicular (**g**) or parallel (**h**) to the membrane plane. **i**. Domain II of the $Ca_V2.2$ complex, overlaid with an electrostatic potential surface on the VSD_{II}. The putative PIP_2 molecular is shown as spheres.

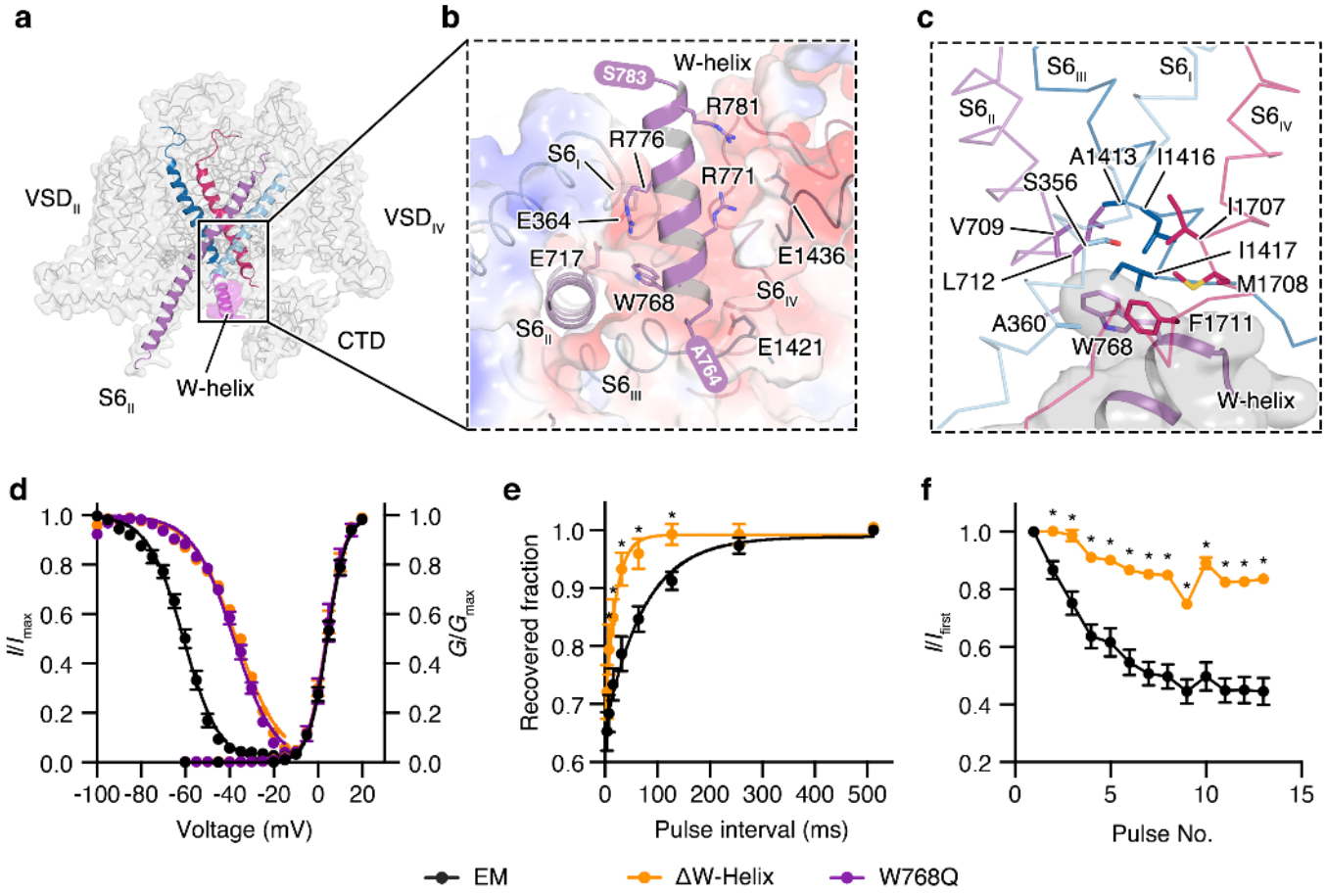

Figure 4. Inactivation mechanism of $Ca_V2.2$ complex.

a. The W-helix is composed of ^{764}ARSVWEQRASQLRLQNLRAS^{783} and determined underneath the intracellular gate of the $Ca_V2.2$. The $Ca_V2.2$ is shown in ribbon and overlaid with transparent surfaces. The S6 helices are shown in cartoon and highlighted. The W-helix is shown in cartoon and overlaid with a transparent surface, colored in purple. **b**. Interactions between the W-helix and the intracellular gate viewed from intracellular side. The critical residues involved in the interactions were shown in sticks. The N- and C-terminus of the W-helix is indicated. **c**. The W768 from W-helix stabilized the intracellular gate at closed state. The S6 helices are shown as ribbon. The W-helix is shown in cartoon and overlaid with a transparent grey surface. **d.** Steady-state activation and inactivation for the $Ca_V2.2^{EM}$ complex and its mutants. (Activation: EM, n = 13; ΔW-helix, n = 8; W768Q, n = 6; Inactivation: EM, n = 8; ΔW-helix, n = 6; W768Q, n = 6) **e.** Recovery of close-state inactivation for the $Ca_V2.2^{EM}$ complex and its mutants. Cells were held to –40 mV for 200 ms, and then stepped to –100 mV for indicated time delay (4-512 ms), followed by a +10 mV test-pulse (35 ms) (EM, n = 7; ΔW-helix, n = 8). **f.** Ratio of Cav2.2 channels inactivation calculated from the first spike eliciting maximal current to the other spikes in the AP trains (EM, n = 8; ΔW-helix, n = 6). Black, $Ca_V2.2^{EM}$ complex; purple, W768Q; orange, ΔW-helix. * indicates $p < 0.05$.